UC San Diego
UC San Diego Previously Published Works

Title

Fractional change of scattering and absorbing aerosols contributes to Northern Hemisphere Hadley circulation expansion.

Permalink

Journal

Science Advances, 10(46)

Authors

Ying, Tong

Li, Jing

Fu, Qiang

et al.

Publication Date

2024-11-15

DOI

10.1126/sciadv.adq9716

Peer reviewed

ATMOSPHERIC SCIENCE

Fractional change of scattering and absorbing aerosols contributes to Northern Hemisphere Hadley circulation expansion

Tong Ying[1,2]†, Jing Li[1,2]*, Qiang Fu[3], Guanyu Liu[1,2], Lu Zhang[1,2]‡, Yan Xia[4], Yongyun Hu[1,2]*

The relative amount of scattering and absorbing aerosols is essential in determining the aerosol radiative and climate effects. Using reanalysis datasets and climate simulations, here, we show that changes in the relative amount of scattering and absorbing aerosols in the Northern Hemisphere (NH) high latitudes, manifested as long-term decreasing trends in aerosol single-scattering albedo (SSA), have played an important role in driving the widening and weakening trends of the NH Hadley circulation (HC) since the early 1980s. Decreasing SSA in the NH middle and high latitudes can notably warm the troposphere there, thus reducing the equator-to-pole temperature gradient, increasing static stability in mid-latitude regions, and leading to the widening and weakening trends of NH HC. Further analysis of the Coupled Model Intercomparison Project Phase 6 (CMIP6) aerosol forcing–only simulations also supports the importance of SSA trends in perturbing NH HC through the above mechanism.

INTRODUCTION

The Hadley circulation (HC) is one of the major large-scale circulation systems in which moist warm air ascends in deep tropics, diverges poleward in the upper troposphere, and sinks in the subtropical regions (1). HC is essential to the energy and moisture transport among different latitudes and is dominant in determining climates in tropical and subtropical zones. Since the start of satellite era, an HC expansion has been observed in both hemispheres (2–5), which has profound impacts on people living in tropical and subtropical regions, accounting for nearly half of the world's population. This tropical expansion, substantially appearing in the autumn in both hemispheres (2, 5–7), has been attributed to the changes of atmospheric eddies due to altered meridional and vertical temperature structure (8), which has been linked to natural variability (9–12) and human activities (13), including the increase of greenhouse gasses (GHGs) (14–17), the decrease of stratospheric ozone (18–21), and the change of volcanic (22) and anthropogenic aerosols (9, 23).

Among all the above potential drivers of HC expansion, anthropogenic aerosol is the most uncertain. Because of the complexity of their composition, forcing mechanisms, and the spatial-temporal distribution, aerosols contribute the largest uncertainty to anthropogenic radiative forcing (24), let alone the uncertainties in temperature, precipitation, and large-scale circulation changes (25, 26). The heating effect due to black carbon aerosols has been recognized to have a nonnegligible impact on the HC expansion in the Northern Hemisphere (NH) (23). However, in real world, the effect of absorbing aerosols must be considered together with scattering aerosols, and

the competition between the cooling effects of scattering aerosols and the warming effects of absorbing aerosols (27) further complicates the role of aerosols in the poleward shift of the tropical boundary (28). The relative fraction of scattering and absorbing aerosols is typically quantified by the single-scattering albedo (SSA) parameter, and a lower SSA suggests higher absorbing aerosol fraction and vice versa. Previous studies on the aerosol climate effects often considered the total amount (9, 29–31) or single species (23, 32, 33), yet the changes of SSA along with its impact on large-scale circulation have not been estimated. The role of SSA change in the tropical expansion could give us new insight to the effects of aerosol compositional change alongside the change of aerosol total loading, which has not been explicitly investigated in previous studies.

In this study, we systematically analyze the contribution of changes in the relative amount of scattering and absorbing aerosols through SSA to the HC expansion in the NH over the past four decades by comparing to the effect of total aerosol loading change through the aerosol optical depth (AOD), as well as the effect of GHGs. A set of numerical experiments using the Community Earth System Model (CESM) version 1.2.2 with aerosol mass concentration fields prescribed by the Modern-Era Retrospective analysis for Research and Applications, version 2 (MERRA-2) reanalysis data is performed to examine the impacts of SSA and AOD changes separately. The outputs from Coupled Model Intercomparison Project Phase 6 (CMIP6) aerosol forcing–only (hist-aer) simulations are also analyzed to estimate the response of NH HC to aerosol forcing.

RESULTS

Comparison between observed and simulated HC changes

Here, we focus on the NH where aerosol emissions are much more intense than the Southern Hemisphere. We quantify the width of HC through several commonly used metrics (4, 6, 8, 34), namely, (i) Ψ_{500}: latitude where the zonal mean meridional mass streamfunction (MMS) at 500 hPa changes from positive to negative, (ii) eddy-driven jet (EDJ): latitude of the maximum zonal mean zonal wind at 850 hPa, (iii) sea level pressure (SLP): latitude of the maximum zonal mean SLP in the subtropics, (iv) U_{srf}: latitude where zonal

[1]Department of Atmospheric and Oceanic Sciences, School of Physics, Peking University, Beijing, P. R. China. [2]Laboratory for Climate and Ocean-Atmosphere Studies, Department of Atmospheric and Oceanic Sciences, School of Physics, Peking University, Beijing, P. R. China. [3]Department of Atmospheric Sciences, University of Washington, Seattle, WA, USA. [4]School of Systems Science, Beijing Normal University, Beijing, P. R. China.
*Corresponding author. Email: jing-li@pku.edu.cn (J.L.); yyhu@pku.edu.cn (Y.H.)
†Present address: Scripps Institution of Oceanography, University of California San Diego, San Diego, CA 92037, USA.
‡Present address: Key Laboratory of Radiometric Calibration and Validation for Environmental Satellites, National Satellite Meteorological Center (National Center for Space Weather), China Meteorological Administration, Beijing, China.

mean surface zonal wind transitions from easterlies to westerlies, and (v) outgoing longwave radiation (OLR): first latitude where OLR drops to 20 W/m² below the peak value poleward of the subtropical OLR maximum. The NH HC edges obtained from these five metrics are also averaged into a combined metric named "ALL." Figure 1 (A and B) compares the seasonal and annual mean trends of the NH HC edge from the early 1980s to 2022 between reanalysis datasets and numerical experiments forced by aerosol and GHG changes since the early 1980s using the CESM (see Materials and Methods). Consistent with previous studies (*4*, *35*), both the European Centre for Medium-Range Weather Forecasts Reanalysis version 5 (ERA5) and MERRA-2 indicate a NH tropical expansion in the boreal autumn [September to November (SON)] based on all the five metrics and the combined ALL metric (Fig. 1A). The tropical NH boundary from the ALL metric is shifted by 0.31° per decade for 1979–2022 in ERA5, and 0.48° per decade for 1980–2022 in MERRA-2, both statistically significant. The AER and SSA experiments of CESM simulations, representing the responses to changes in total aerosols and changes in the relative amount of scattering and absorbing aerosols, reproduce significant SON widening trends based on EDJ, SLP, U_{srf}, and OLR and insignificant positive trends based on Ψ_{500}, whereas the AOD experiment, representing the responses to changes in aerosol total loading, yields significant widening trends only based on OLR but insignificant widening trends for the other metrics, implying that SSA change has greater contribution to the total effect of aerosols compared to AOD change. The other two experiments yield weak or reversed trends for the NH HC edge, especially based on EDJ, SLP, and U_{srf} (Fig. 1A). Figure 1B shows the seasonal and annual trends based on the ALL metric, whereas the results of other metrics are shown in fig. S1. In the AER experiments, the ALL metric shows the strongest and most notable poleward displacement of the NH HC boundary in SON by 0.24° per decade, and the AOD and SSA experiments also show significant widening trends in SON based on the ALL metric by 0.15° and 0.17° per decade, respectively (Fig. 1B), indicating that, compared to AOD change, SSA change contributes a slightly larger part to the response of the NH HC edge to aerosol forcing, accounting for about 73% of the signal in the AER experiment. The GHG + AER and GHG experiments, representing the combined effects of GHGs and aerosols as well as the GHG effect alone, yield insignificant trends in SON based on all the six metrics (Fig. 1A). Although the GHG + AER experiment indicates significant widening trends in the boreal summer [June to August (JJA)], the overall responses to GHG forcing in our simulations appear weaker than ERA5/MERRA-2 reanalysis (Fig. 1B), or previous studies suggesting positive contributions of GHGs to the expansion trend (*14*, *15*, *36*). This inconsistency might be due to the relatively weaker forcing since we focus on observed CO_2 change in a 37-year period rather than 1% CO_2 increase per year or abrupt four times CO_2 increase used in the previous studies, while lack of full ocean dynamics in our simulations might also play a role. Meanwhile, the response in the GHG + AER experiment is much weaker than the sum of GHG and AER experiments, implying a nonlinear relationship between aerosol and GHG forcing.

Along with the expansion, the strength of NH HC in SON, defined as the maximum absolute value of zonal mean MMS at 500 hPa, also shows a weakening by 2.2×10^9 and 1.2×10^9 kg/s per decade according to ERA5 and MERRA-2, respectively (Fig. 1C). This weakening trend could be captured by the AOD, SSA, GHG + AER, and GHG experiments, albeit with underestimated amplitudes of
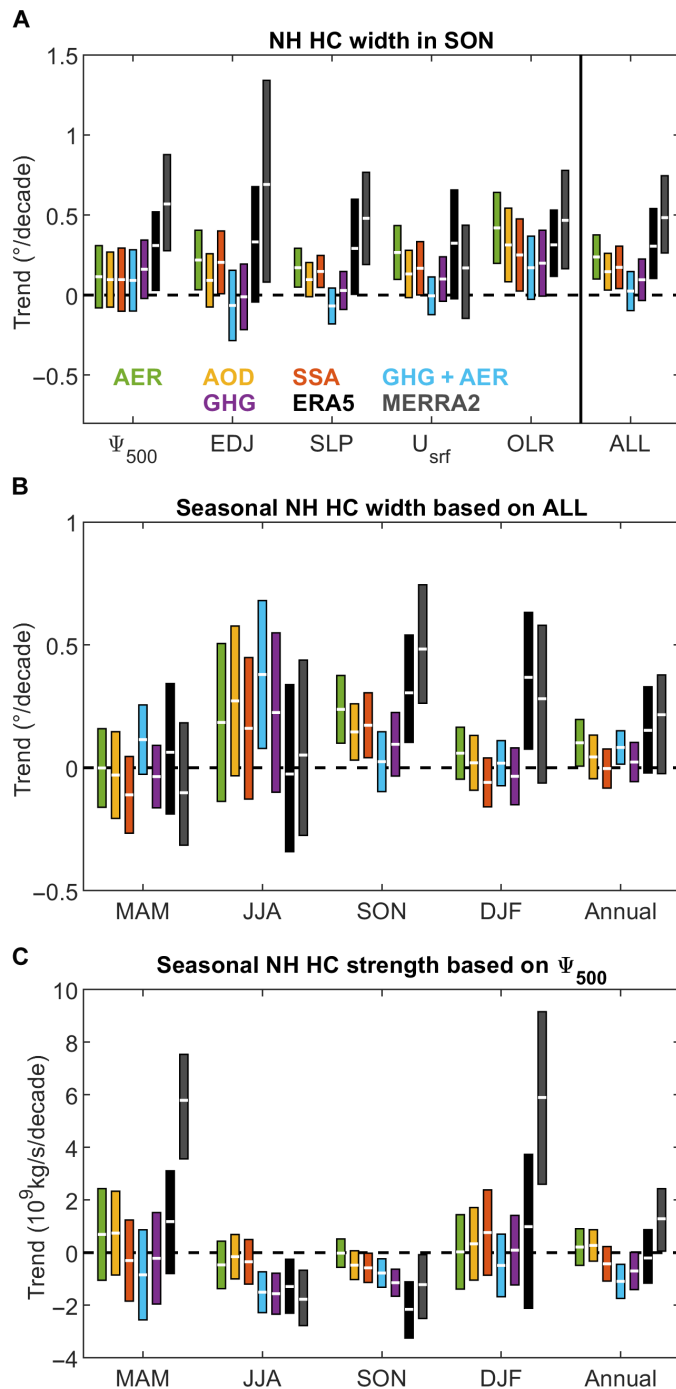
Fig. 1. Observed and simulated NH HC boundary displacement and strength change from the early 1980s to the present. (**A**) SON mean poleward displacement of five metrics, as well as ALL. (**B**) Poleward displacement of the NH HC edge by season based on the combined ALL metric. (**C**) NH HC strength change by season based on the zonal mean MMS at 500 hPa. The differences between simulations forced by 1980–1984 and 2017–2021 conditions are converted into trends (degrees per decade and 10^9kg/s per decade) assuming a time period of 37 years (see Materials and Methods). The white centered lines with colored boxes represent the mean response of each experiment with its confidence intervals at 95% confidence level according to a two-sample *t* test. The black and gray boxes show the HC boundary trends observed by reanalysis datasets, in which the linear trends are calculated by Sen's slope, and the 95% confidence intervals are calculated by the Mann-Kendall test. MAM, March to May; DJF, December to February.

0.47×10^9, 0.58×10^9, 0.77×10^7, and 1.14×10^9 kg/s per decade, respectively, indicating that GHG change is effective in causing the weakening trends of NH HC, and AOD and SSA change also have their contributions. A significant weakening trend could also be observed in JJA, which is captured by the GHG + AER and GHG experiments. These results are consistent with previous studies showing model-projected weakening of the atmospheric circulations in response to warming (*37*, *38*). In boreal spring (March to May) and winter (December to February), MERRA-2 exhibits significant strengthening trends, whereas these signals fail to appear in ERA5 data or CESM simulations. Note that the capability of reanalysis datasets to capture the recent weakening trend of NH HC seems limited due to artificial biases, but the weakening trend itself has been confirmed by observations (*13*).

In sum, comparison between reanalysis and CESM simulations indicates that since the beginning of the satellite era, NH HC has experienced robust widening and weakening trends in boreal autumn. The simulations indicate that, compared to the effects of GHGs, aerosol changes could induce a stronger widening trend. Furthermore, changes in the relative amount of absorbing and scattering aerosols appear to be an important contributor to the responses to aerosol changes, accounting for about 73% of the expansion induced by aerosols and about 55 and 34% of the NH HC boundary displacements derived from ERA5 and MERRA-2, respectively. The changes in the relative amount of absorption and scattering could also contribute to the NH HC weakening trends by 27 and 48% compared to the trends of ERA5 and MERRA-2, respectively. Although there exists an overlap between the confidence intervals derived from the AOD and SSA experiments, which is due to the uncertainties of the NH HC boundary itself, the effects of AOD and SSA changes are better separated by performing a bootstrapping test (fig. S2), especially based on the EDJ and SLP metrics (fig. S2A). These results indicate that, compared to the effect of aerosol total loading change alone, changes in the aerosol absorption/scattering property associated with aerosol compositional change could induce a comparable or even stronger perturbation to NH HC in boreal autumn.

Mechanism of scattering and absorbing aerosol relative amount changes in driving HC expansion

To understand the mechanisms for aerosol forcing to affect NH HC in SON, we further examine the responses of meteorological fields. Figure 2 shows the simulated AOD and SSA changes from the early 1980s (1980–1984) to the early 2020s (2017–2021) driven by the aerosol mass concentration fields derived from MERRA-2 (see Materials and Methods). Compared to the early 1980s, the AOD at the present day increases in developing regions, including Eastern China, South Asia, Amazon, and the southern part of Africa, and decreases in developed regions, such as Europe and North America (Fig. 2A), implying a redistribution of emissions in the past few decades. Meanwhile, SSA increased over East Asia, South Asia, and the Middle East, implying decreased absorbing aerosol fraction, whereas it significantly decreases in the mid- to high-latitude regions, which are associated with increased absorbing aerosol fraction (Fig. 2B). Black carbon mainly increases over East and South Asia, slightly increases in North America, and decreases in Europe (fig. S3D), causing an increase of zonal mean absorbing AOD in NH (fig. S4G). Sulfate aerosols change more sharply (fig. S3A), as indicated by the increased scattering AOD in the low latitudes and decreased scattering AOD in the mid-to-high latitudes (fig. S4D). There is thus an

increase in the relative fraction of aerosol scattering in East and South Asia but a decrease in Europe and North America (Fig. 2B). Note that the changes of AOD and SSA could be significant over some remote ocean basins, as this is a difference test rather than a trend test (see Materials and Methods).

By scaling the climatological aerosol mass concentration fields, the AOD experiment shows the same AOD trend pattern as the AER experiment (Fig. 2, A and C), while its SSA remains largely unchanged (Fig. 2D). All aerosol species in the AOD experiment are scaled with the same factor (fig. S3; see Materials and Methods), and the zonal mean scattering and absorbing AOD trends show similar patterns (fig. S4, E and H). On the other hand, the SSA experiment successfully produced a similar SSA trend pattern as the AER experiment (Fig. 2, B and F), while its AOD remains largely unchanged (Fig. 2E). In the SSA experiment, reduction of sulfate in the mid-to-high latitudes is balanced by the increase of absorbing aerosols (fig. S3), resulting in a small change in total extinction but a significant increase in aerosol absorption (fig. S4, C and I). The simulated AOD and SSA trends in different experiments confirm that our experimental design has successfully isolated the AOD and SSA forcing.

Figure 3 shows the changes of NH zonal mean MMS, potential temperature, and zonal wind in response to all-aerosol, AOD, and SSA changes. The responses of zonal mean MMS show similar patterns in all three experiments but with slightly different magnitudes and distributions (Fig. 3, A to C). The decrease of zonal mean MMS around 15°N corresponds to the weakening trend of the NH HC, and the increase of MMS from 30° to 40°N, which sits right at the northern edge of HC, suggests a poleward shift. The positive MMS trend over the subtropics in the AER and SSA experiments extends more poleward relative to the zero MMS line than that in the AOD experiment. Meanwhile, the maximum positive MMS trends occur on the poleward side of the zero MMS line in the SSA experiment but on the equatorward side in the AER and AOD experiments. All three experiments show negative MMS trends in the center of NH HC, especially in the AOD and SSA experiments. Using the Kuo-Eliassen (KE) equation (see Materials and Methods), the trends of MMS induced by aerosol forcing are decomposed into contributions of diabatic heating, eddy fluxes, zonal friction, static stability, and residual terms (figs. S5 to S7). Consistent with previous studies (*16*, *39*), the diabatic heating related to the latent heat process dominates the weakening trend of NH HC, and the positive trends of MMS near the NH HC edge are mainly due to changes in the eddy fluxes with contributions from latent heating, radiative heating, and zonal friction. The eddy heat flux term in the AOD experiment contributes negatively to the zonal mean MMS (fig. S6E), whereas the AER and SSA experiments both have positive contributions to the clockwise circulation anomalies (figs. S5E and S7E), leading to the widening trend of NH HC. Meanwhile, zonal mean MMS anomalies induced by the eddy momentum flux term in the AER and SSA experiments also distribute more poleward compared to that in the AOD experiment (figs. S5F, S6F, and S7F). As a result, the overall zonal mean MMS anomalies associated with both total aerosol and SSA changes show significant positive trends near the edge of NH HC, indicating stronger widening trends than that corresponds to AOD change (Fig. 3, A to C). Note that the contributions from these physical processes are not independent. These MMS trends are consistent with the results of the expansion defined by the Ψ_{500} metric, confirming that change in the relative fraction of scattering and absorbing aerosols has non-negligible contribution to the aerosol-induced NH HC change.
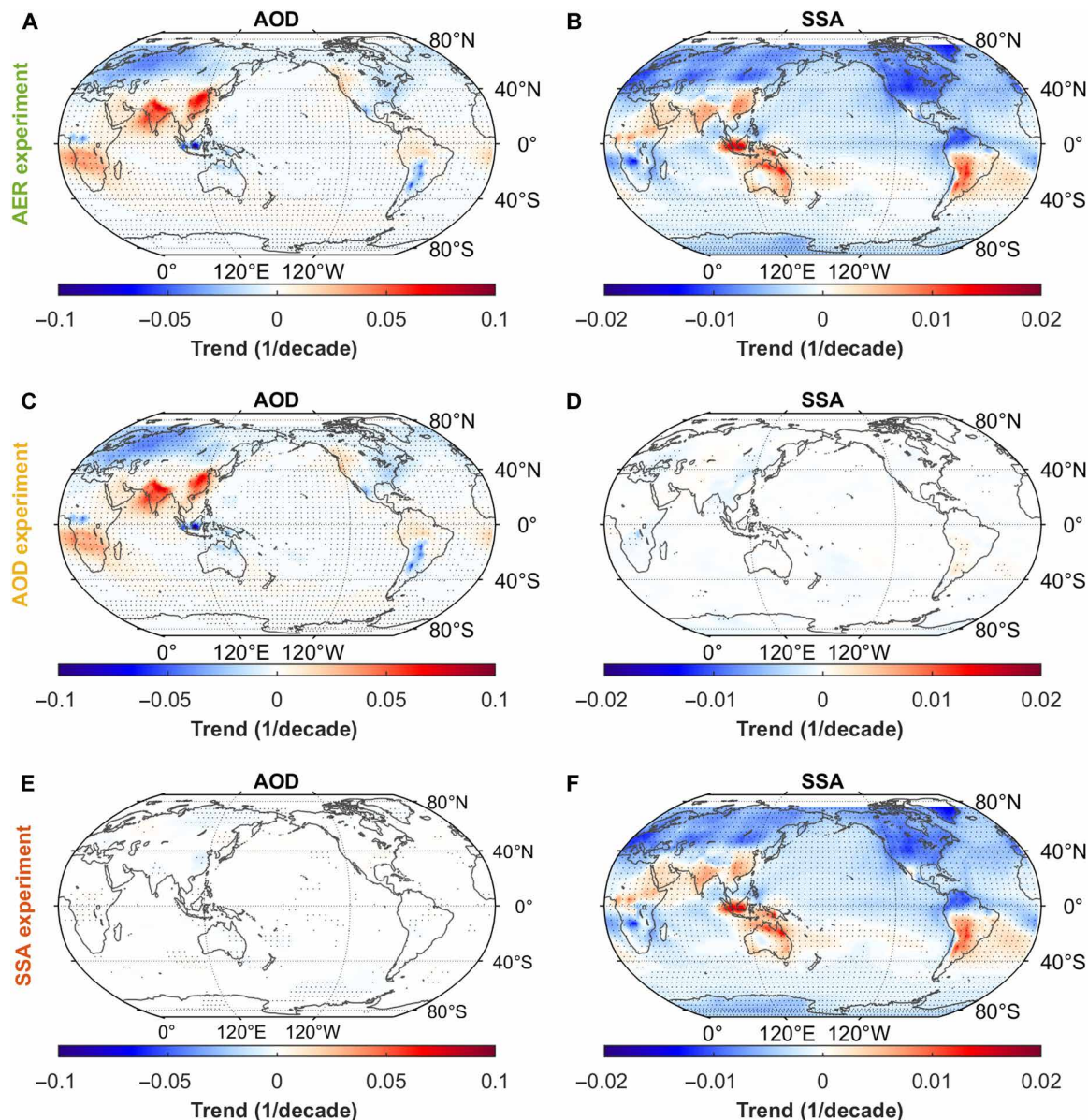
Fig. 2. Simulated AOD and SSA changes in boreal autumn from the early 1980s (1980–1984) to the present (2017–2021) in CESM experiments. (A and **B)** AOD and SSA trends in the AER experiment, respectively. (**C** and **D)** Same as (A) and (B) but for the AOD experiment. (**E** and **F)** Same as (A) and (B) but for the SSA experiment. Differences between simulations are converted into decadal trends assuming a period of 37 years. Grid boxes with black dots pass the two-sample *t* test at 95% confidence level.

Changes of HC are typically linked to the changes of meridional temperature gradient, subtropical stability, and subtropical jet stream (*14*, *36*, *40*). In all three experiments, warming signals appear in the lower to mid-atmosphere (900 to 100 hPa) over the mid-latitudes (30° to 60°N). This warming signal is strongest in the SSA experiment and occurs throughout the column (Fig. 3F), whereas the AOD experiment shows much weaker and insignificant warming in the upper level over mid-latitudes and significant cooling from surface to mid-troposphere over the low latitudes (Fig. 3E). The AER experiment shows comparable warming signal to that of the SSA experiment in mid- to high-latitude troposphere and significant surface cooling signal similar to that of the AOD experiment (Fig. 3D),

which could be directly linked to the meridional structure of scattering and absorbing AOD (fig. S3) and related changes of diabatic heating (fig. S8). In NH mid-to-high latitudes, aerosol forcing directly induces changes of shortwave heating rate (fig. S8, D to F) with negligible trends in the longwave heating rate, in response to the warming signal in the AER and SSA experiments (fig. S8, G and I). In addition, the negative trends of the latent heating rate indicate the expansion of the tropical dry zone (fig. S8, A to C). Trends of sea surface temperature (SST) also indicate that SSA change dominates the warming signals in northern Pacific (fig. S9, A, C, and E). Both warming over the mid-latitudes and cooling over the low latitudes suggest a decrease in the meridional temperature gradient.
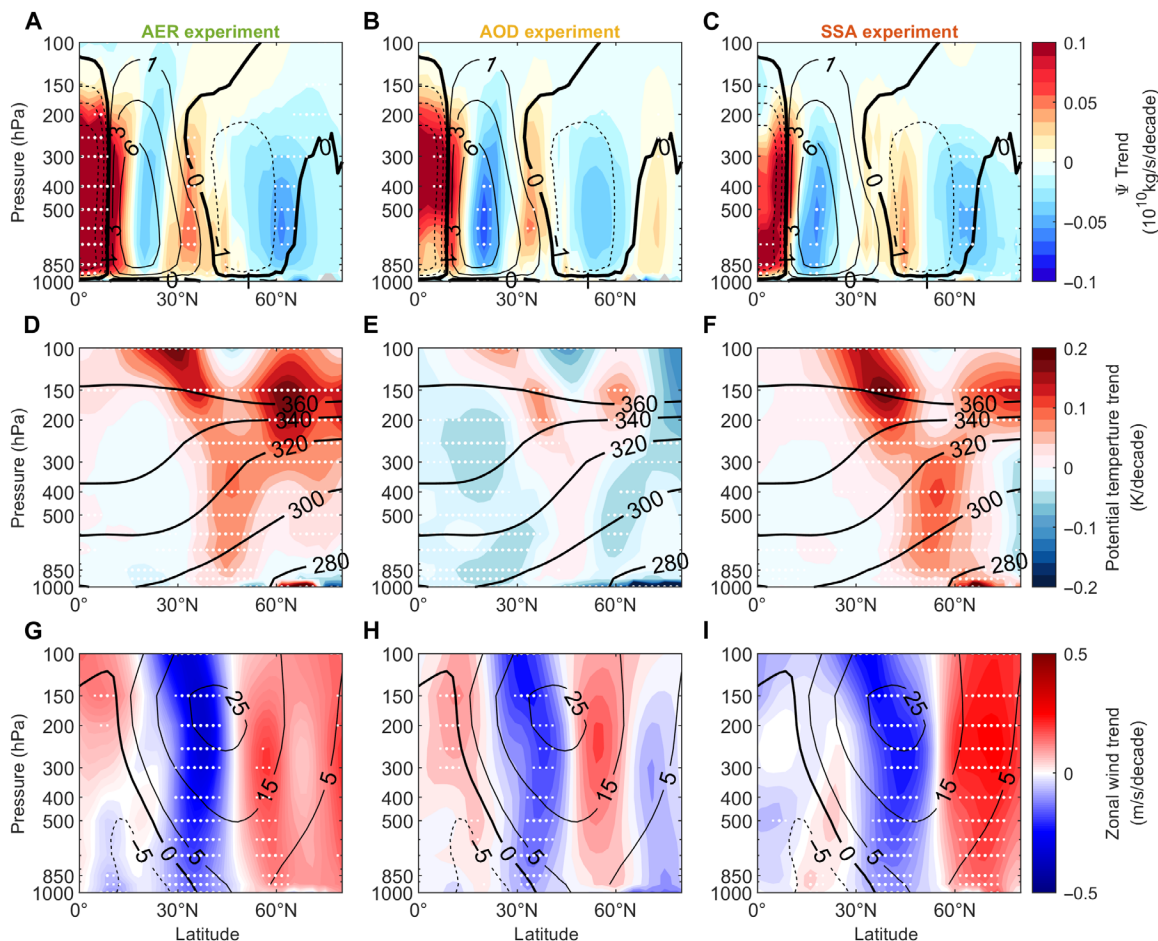
Fig. 3. Trends of NH zonal mean MMS, potential temperature, and zonal wind in boreal autumn in different aerosol forcing experiments. (**A**, **D**, and **G**) Trends of zonal mean MMS, potential temperature, and zonal wind in the AER experiment. (**B**, **E**, and **H**) Same as (A), (D), and (G) but for the AOD experiment. (**C**, **F**, and **I**) Same as (A), (D), and (G) but for the SSA experiment. Color scales represent trends of zonal mean MMS, potential temperature, and zonal wind, and contours represent their mean state in the forced simulation by the 1980–1984 condition. The units of the contours are 10^{10} kg/s, degrees Celsius, and meters per second, respectively. Grid boxes with big white dots are regions that have statistical significance above the 95% confidence level, and regions with small white dots are above the 90% confidence level.

Meanwhile, changes in the vertical structure of temperature induce the significant positive trends of static stability near the subtropical tropopause in the AER and SSA experiments (fig. S10, A and C), allowing the poleward flow in the upper troposphere to reach higher latitudes before it becomes unstable, which is accompanied by increased eddy momentum flux in the mid-to-high latitudes (fig. S10, J and L). The subtropical jet thus shows a weakening trend and a poleward displacement in response to aerosol forcing as seen from the trends of the zonal mean zonal wind (Fig. 3, G to I). Zonal wind in all three experiments shows similar decreasing trends equatorward to the maximum westerlies at 850 hPa, while on the poleward side, the increasing trends are significant in the AER and SSA experiments but not in the AOD experiment, so that the AER and SSA experiments show stronger expansion than the AOD experiment based on the EDJ metric. Zonal wind is also more sensitive in the AER experiment than in the AOD and SSA experiments near the zero point near the surface where easterlies transit to westerlies, which is consistent with the results of the U_{srf} metric. The response of SLP in the AER experiment is significantly positive in NH mid-to-high latitudes, and SSA change contributes the main

part of the signals in northern Pacific (fig. S9, B and F), leading to the HC widening trends based on the SLP metric. The above results indicate that changes in the relative fraction of scattering and absorbing aerosols contribute a larger part to the effects of aerosol forcing in altering the atmospheric thermodynamic structure than changing the total aerosol amount alone.

The increase of aerosol absorption itself, as emphasized by previous studies (*23*), could not explain the widening signals in the AER experiment. Although the increase of absorbing AOD appears in almost the entire NH (fig. S4G), the temperature change is obviously different between low and mid-latitudes. In low-latitude regions where scattering aerosols increase more than absorbing aerosols, as manifested by an SSA increase, the warming effect of absorbing aerosols is completely offset by the cooling effect of scattering aerosols, whereas in the mid-to-high latitudes where scattering aerosols significantly decrease, the warming effect dominates the temperature change (Fig. 3D and fig. S4, D and G). This warming signal is even stronger in the SSA experiment (Fig. 3F), in which AOD in the mid-to-high latitudes remains at a relatively high level (1980–1984). On the other hand, the cooling signal of the AOD

experiment (Fig. 3E) in the low latitudes is also stronger than that in the AER experiment where SSA in the low latitudes remains at a lower level (1980–1984). A few studies have reported that aerosol radiative forcing is more sensitive to the change of SSA when AOD is high, whereas it is more sensitive to AOD change when SSA is low (*41–43*), since AOD describes the total extinction of aerosols and SSA stands for the relative fraction of scattering to extinction. Consistent with these studies, our results indicate that temperature structure is also sensitive to SSA changes when AOD is fixed at a relatively high level (1980–1984), whereas it is more sensitive to AOD changes when SSA is fixed at a relatively low level (1980–1984). In addition, we also tested the effects of AOD and SSA changes with the other factor fixed at 2017–2021 level rather than at 1980–1984 level, and the response of NH HC expansion in SON to AOD and SSA changes is slightly reduced (Fig. 1B and fig. S11), indicating the limited impact of the nonlinear effects of AOD and SSA on our results.

HC expansion in response to aerosol forcing in CMIP6 simulations

Considering that aerosol-cloud interaction, especially the Twomey effect, is not included in the CESM Community Atmosphere Model version 4 (CAM4) simulations, and that our simulations are based on the equilibrium response to aerosol forcing with the lack of ocean dynamics, it is necessary to further compare the transient responses of HC to aerosol forcing in fully coupled and more state-of-the-art models. As reported in previous studies, the multimodel mean result from the CMIP6 hist-aer experiment shows a little widening trend of NH HC (*44*, *45*). However, trends among different models show large diversity. This diversity comes from different responses to aerosol forcing in different models, as well as the uncertainties of aerosol forcing themselves. To further understand the relationship between HC expansion and aerosol changes, here, we collect eight

models (table S2) providing a complete output of hist-aer simulations, including meteorological fields, aerosol optical properties including AOD and absorbing AOD (used to calculate SSA), as well as cloud microphysical properties such as cloud droplet number concentration (CDNC), and then their performances are compared.

Figure 4 compares the simulated displacement of the NH HC edge based on the Ψ_{500} metric and SSA trends averaged from 45° to 60°N, trends of static stabilities defined as the difference between the potential temperature at 400 and 850 hPa averaged from 30° to 50°N, and trends of meridional temperature gradient defined as the difference of 850-hPa temperature between 0° to 20°N and 40° to 70°N from 1980 to 2014 in hist-aer simulations. The trends of the NH HC edge derived from CMIP6 hist-aer simulations correlate well with the SSA trends in mid-to-high latitudes, and models with stronger decreasing trends of SSA tend to simulate stronger expansion of NH HC (Fig. 4A). Among all the selected CMIP6 models, CESM2 indicates the strongest widening trend of NH HC, reaching up to 0.59° per decade, which might come from its most significant decreasing trend of SSA in NH mid-to-high latitudes. The results of CESM2 appear much stronger than that of our CESM1 simulations with similar NH mid- to high-latitude SSA trends, which might be due to the lack of ocean dynamics in our simulations. Also, CESM2 is the only model that captures the SSA trend and the NH HC trend revealed by MERRA-2 reanalysis. We therefore consider that the results of CESM2 might better represent the physical relationship between aerosol forcing and HC expansion. HC expansion signals simulated by different models also correlate well with the changes of static stabilities in mid-latitude regions as well as the meridional temperature gradient, indicating that both processes could contribute to the expansion of NH HC in response to aerosol forcing (Fig. 4, B and C).

Note that large uncertainties exist in the simulated aerosol trends, especially those for SSA. The AOD trends simulated by
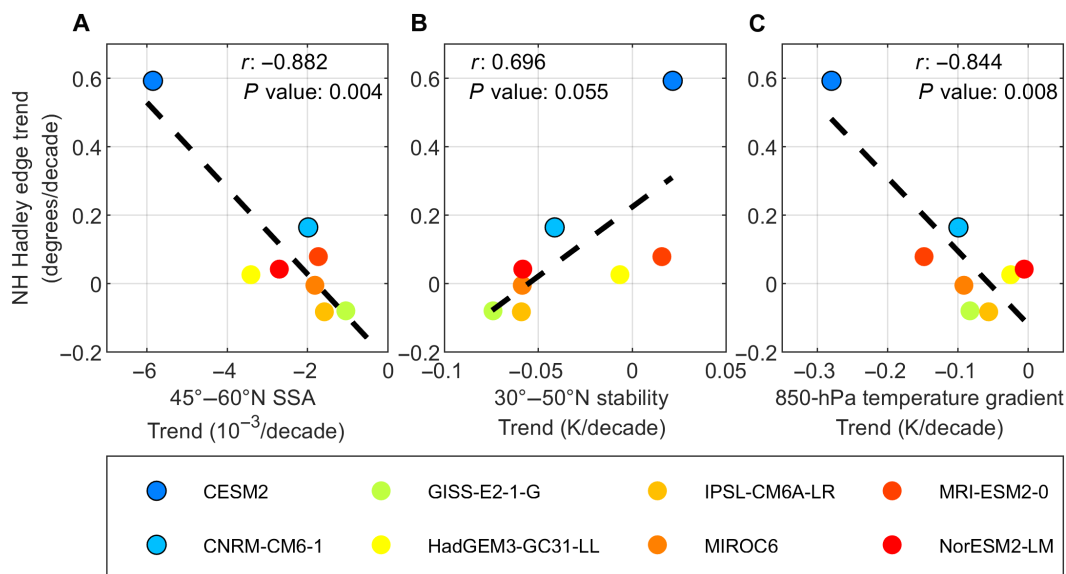
Fig. 4. Relationship between NH HC expansion in boreal autumn (SON) and SSA, mid-latitude stability, and meridional temperature gradient derived from CMIP6 hist-aer simulations. (**A**) Relationship between NH HC expansion and 45° to 60°N SSA trends. (**B**) Relationship between NH HC expansion and 30° to 50°N static stability trends. (**C**) Relationship between NH HC expansion and 850-hPa meridional temperature gradient trends. Circles with a black edge represent that the trends of the NH HC edge indicate significance at 95% confidence level, and the black dotted lines represent linear regression of all model results.

CMIP6 models show similar spatial patterns with decreases in Europe and North America and increases in East and South Asia, but the magnitudes of AOD change simulated by different models show large spread (fig. S12). Compared to the Aerosol Robotic Network (AERONET) level 2.0 monthly AOD product, most of the models overestimate the AOD decrease in the mid-to-high latitudes, and among all these models, CESM2 exhibits the best consistency with ground-based observations (fig. S12A). The inconsistency of the simulated SSA trends is more complicated in that not only the spatial patterns disagree but also the absolute values of SSA trends are highly variable (fig. S13). CESM2 successfully captures the strong decreasing trend of SSA in mid-to-high latitudes, although it failed to capture the SSA increase in East and South Asia. Such uncertainties of aerosol forcing, especially the inconsistencies of SSA trends, are very likely one of the causes contributing to the large spread of the simulated displacement of the NH HC boundary, ranging from −0.08° to 0.59° per decade.

To further confirm whether aerosol-cloud interactions, particularly the Twomey effect, have notable impacts on the simulated NH HC expansion, the trends of low CDNC simulated by CMIP6 models are compared (fig. S14). Their spatial patterns are consistent with that of AOD trends, indicating that the decrease of aerosols in mid-to-high latitudes and the increase of aerosols in low-latitude regions can affect CDNC, inducing changes of cloud albedo and reducing the meridional temperature gradient. However, trends of meridional temperature gradient in models with strong CDNC trends are much weaker compared to that of CESM2 (Fig. 4C), implying that cloud microphysical property change is unlikely the dominant factor of the warming signal in mid-to-high latitudes. Meanwhile, the decreased low cloud albedo in mid-to-high latitudes could decrease the aerosol absorption above, which is not conductive to the increase of static stability. Among all the models, CESM2 and IPSL-CM6A-LR have more accurate AOD trends compared to observations (fig. S12, A and E) as well as similar CDNC changes (fig. S14, A and E), but the former one indicates the strongest NH HC widening trend, while the latter one shows the weakest trend (Fig. 4), which is possibly caused by their distinct SSA trends, especially the magnitudes of SSA decrease in NH mid- to high-latitude regions (Fig. 4A and fig. S13, A and E).

DISCUSSION
Implications of aerosol forcing and climate change
Anthropogenic aerosols are among the major drivers of climate change. Because of their complicated composition, heterogeneous spatial-temporal distribution, and varied forcing mechanisms, aerosols contribute the largest uncertainties among all the factors in anthropogenic forcing. The radiative forcing of aerosols is related to not only their total amount but also their scattering and absorbing properties, especially because scattering and absorbing aerosols have distinct or even opposite climate effects. Moreover, the relative fraction of scattering and absorbing aerosols changes with time (46), implying a change in aerosol forcing even without significant changes in the total aerosol loading, a factor not yet explicitly investigated before. Our study suggests that changes in the relative amount of scattering and absorbing aerosols are important in perturbing the global energy balance and large-scale circulation, which even exceeds the effect of changing total aerosol loading. Meanwhile, although absorbing aerosols such as black carbon increase mostly in

East Asia and South Asia, the warming effect mainly distributes in mid-to-high latitudes where scattering aerosols decrease, indicating that rather than the change of black carbon itself, the scattering/absorbing fraction change is the dominant factor that decides the optical properties of aerosols as well as their impacts on temperature gradients and large-scale circulation.

The responses of NH HC to total aerosol, AOD, and SSA changes are summarized in Fig. 5. In boreal autumn, the decreasing trend of SSA dominates the warming signal induced by aerosol forcing in NH mid-latitude troposphere, reducing meridional temperature gradient and enhancing subtropical static stability, which weakens the subtropical jet and induces an anomalous circulation near the boundary of NH HC (Fig. 5, B and D). However, the warming effect is much weaker when AOD decreases along with fixed scattering/absorbing fraction (Fig. 5C). These results indicate that changes in aerosol scattering and absorbing properties, especially in NH mid-to-high latitudes, have important contribution to the expansion of NH HC in boreal autumn. Further analysis of CMIP6 hist-aer simulations also indicates that models with stronger SSA decrease in NH mid-to-high latitudes tend to simulate stronger decrease of meridional temperature gradient and enhance mid-latitude static stability, thus contributing to the expansion of NH HC.

Note that there is strong nonlinearity of GHGs and aerosol forcing, since the sum of the GHG and AER experiment results is not equal to the result of the GHG + AER experiment, and this nonlinearity has also been noticed by previous studies (47, 48). These results indicated that the climate effects of aerosols need to be treated carefully since they depend on the status of the atmosphere and the hydrological cycle (47), which might strongly affect the estimation of aerosol forcing. The role of SSA change in the future might be different from its impacts today along with the changes of aerosol emissions as well as the ongoing global warming, and thus caution should be taken when extending the current results to future climate scenarios.

We choose to use prescribed aerosol mass concentration fields derived from the reanalysis dataset as inputs to CESM, since the change of scattering and absorbing aerosols is not yet well represented by most of the state-of-the-art climate models (49). Comparison of CMIP6 hist-aer simulation indicates that accurate representation of SSA is still difficult for most of the models, which might affect their performance in simulating large-scale circulations. However, the lack of accurate long-term SSA observations in the global scale hinders the evaluation of SSA by reanalysis as well as its simulations by climate models (27), and the uncertainty of SSA change in reanalysis datasets might induce additional bias to our understanding of its climate impacts. This calls for the urgent need to develop measurement techniques to establish global SSA observations. Next-generation satellites with multiangle and polarization designs (50) have the potential to provide global information of SSA (51). This, combined with routine in situ observations and chemical transport models, can form the framework for detailed and accurate global monitoring of aerosol optical properties (52), which will help us to better understand the SSA variability as well as its climate effects.

MATERIALS AND METHODS
Reanalysis datasets
Two reanalysis datasets are used as a proxy of observation, namely, the ERA5 (53) and the MERRA-2 (54). Meridional wind, zonal wind, SLP,
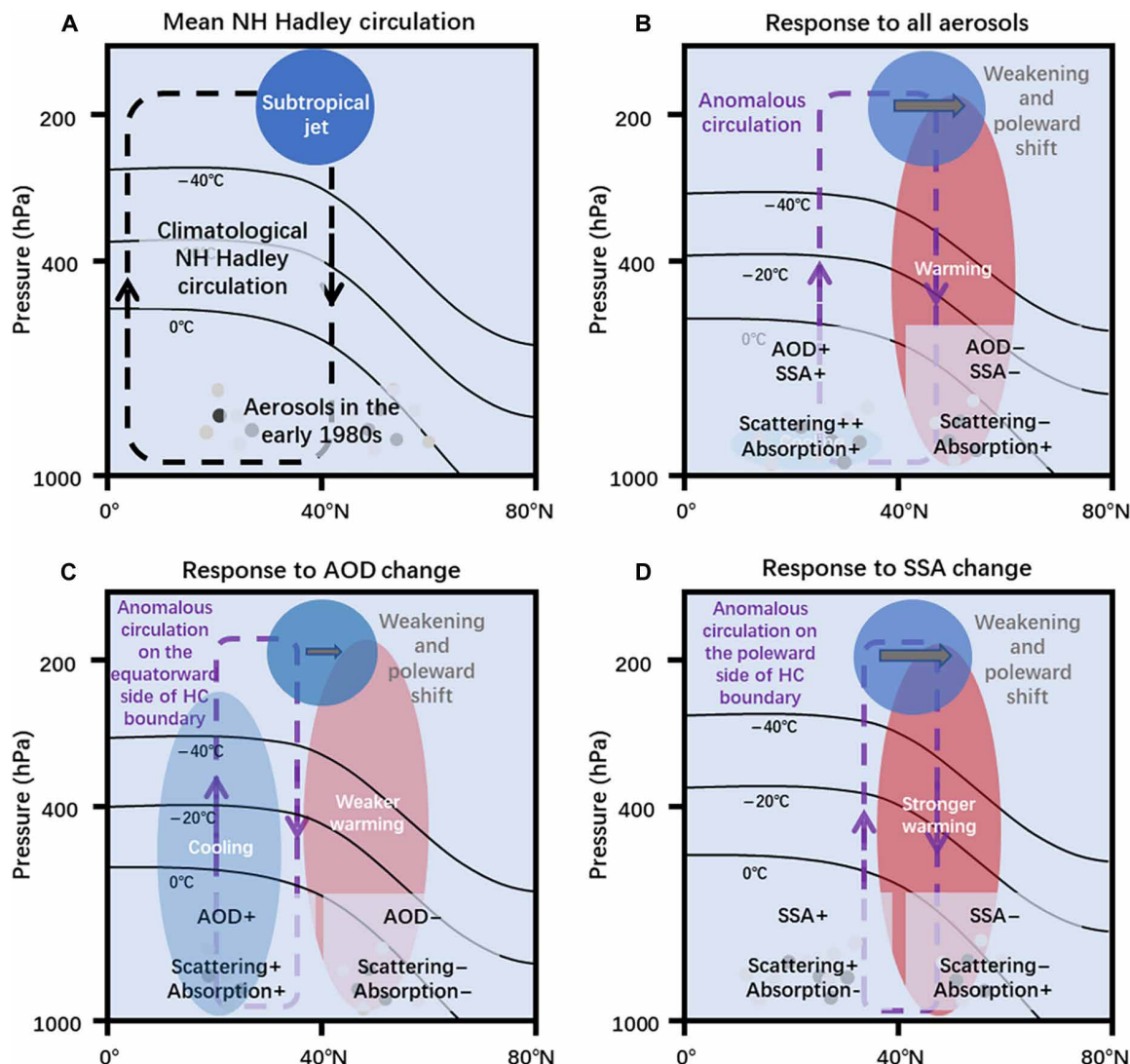
Fig. 5. Schematic of changing NH HC in response to aerosol forcing in boreal autumn. (**A**) Mean state of NH HC. (**B**) Response of NH HC to aerosol forcing since the early 1980s. (**C**) Response of NH HC to AOD change. (**D**) Response of NH HC to SSA change.

and OLR at the top of the atmosphere from these two datasets are collected to be references to the change of HC. The temporal coverage used in our study is 1979–2022 for ERA5 and 1980–2022 for MERRA-2.

Apart from the variables above, aerosol mass concentration fields including sulfate, black carbon, organic carbon, dust, and sea salt from MERRA-2 (*55*) are also used to drive CESM simulations. The averaged aerosol fields from 1980 to 1984 are calculated to represent the aerosols in the early 1980s, and the average from 2017 to 2021 is used to represent the present-day level. To exclude the impacts of volcano activities, especially the eruption of St. Helens in 1980 and El Chichón in 1982, the ratio of sulfate mass concentration at 500 hPa and above in each column of the 1980–1984 average field is scaled to 2017–2021 level so that the stratosphere sulfate is greatly reduced. The fields of sulfate above 500 hPa in 1980–1984 are scaled as

$$mass_{1980-1984,lev<500hPa} = mass_{1980-1984,lev=500hPa}$$
$$\times \frac{mass_{2017-2021,lev<500hPa}}{mass_{2017-2021,lev=500hPa}}$$

Model configurations

For model simulations, the CESM version 1.2.2 (*56*) is used. The atmospheric component is the CAM4, and the oceanic component is the Slab Ocean Model version of Data Ocean Model (DOCN-SOM). In CAM4, the aerosol mass concentration fields of five species, including sulfate, black carbon, organic carbon, dust, and sea salt, are prescribed, so that it is possible to control the change of AOD and SSA by altering the aerosol mass concentration fields. DOCN-SOM is used to reconstruct the response of SST to aerosol forcing, since SST has significant impacts on large-scale circulations. Note that CAM4 includes the direct and semidirect effects of aerosols, whereas the radius of a cloud droplet does not change with aerosols, i.e., the Twomey effect is not considered.

The averaged 1980–1984 level (without volcanic aerosols) and the 2017–2021 level aerosol mass concentration fields from MERRA-2 are interpolated into vertical levels and horizontal grids of CAM4. The vertical interpolation is performed using mass integration between each pressure interface to avoid sampling bias and to keep the

column mass concentration the same as the original MERRA-2 data. The first two simulations are driven by these two fields, namely, aod8084-ssa8084 and aod1721-ssa1721, and the difference between these two simulations is named as the AER experiment, since it represents the contribution of all aerosol changes including both the amount and the scattering/absorbing aerosol fraction from the early 1980s to the present.

The climatology fields of AOD in the first two simulations are obtained to scale the aerosol mass concentration fields in the following experiments. The ratio of AOD in the aod8084-ssa8084 and aod1721-ssa1721 simulations are calculated and then multiplied by the aerosol mass concentration field of the 2017–2021 level, so that the relative fractions of different aerosol species remain at the 2017–2021 level, while the total loading is scaled into the 1980–1984 level. Similar processes are performed to obtain another aerosol mass concentration field where the fraction of each aerosol species is kept at the 1980–1984 level, while the total loading is scaled to the 2017–2021 level. Simulations forced by these two mass concentration fields are named as aod8084-ssa1721 and aod1721-ssa8084 simulations, and their difference from the aod8084-ssa8084 simulation are named as the SSA experiment and the AOD experiment, respectively, for they represent the contributions of SSA and AOD changes with the other parameter fixed at the 1980–1984 level. The aerosol mass concentration fields are constructed as follows

$$mass_{aod8084-ssa1721} = mass_{aod1721-ssa1721} \times \frac{AOD_{aod8084-ssa8084}}{AOD_{aod1721-ssa1721}}$$

$$mass_{aod1721-ssa8084} = mass_{aod8084-ssa8084} \times \frac{AOD_{aod1721-ssa1721}}{AOD_{aod8084-ssa8084}}$$

The concentration of GHGs in the simulations above is controlled at the 2000 level. To further compare the role of aerosols to GHGs, we also perform three simulations in which the aerosols are the same with the first two simulations, while the concentrations of GHGs, including CO_2, N_2O, CFC-11, CFC-12, and CH_4, are set to 1980–1984 and 2017–2021 levels separately; namely, ghg8084-aod8084-ssa8084 simulation, ghg1721-aod1721-ssa1721 simulation, and ghg1721-aod8084-ssa8084 simulation, and the differences of the latter two simulations from the first one are named as the GHG + AER and GHG experiments, representing the combined contribution of changing GHGs and aerosols, and the effects of GHGs, respectively. The GHG concentrations are obtained from National Oceanic and Atmospheric Administration (NOAA) Global Monitoring Laboratory datasets (57–61), in which the observations of CO_2, CFC-11, CFC-12, and N_2O started at least in the late 1970s, while the time series of CH_4 started in the mid-1980s, so we use linear extrapolation to obtain the 1980–1984 level of CH_4.

The summary of all simulations is presented in table S1. All aerosol mass concentration fields are scaled globally. The horizontal resolution of CAM4 is set as 2.5° × 1.9°, and each simulation is performed to a 40-year range in which the first 10 years are treated as the spin-up period.

CMIP6 model simulations
Monthly outputs from the CMIP6 (62) are used to examine the possible linkage between HC change and aerosol forcing. Our study mainly focuses on the hist-aer simulations, in which anthropogenic aerosol and their precursors are the major forcing drivers (63). Only eight models provide complete outputs of AOD, absorbing AOD, and CDNC, and their temperature and meridional winds are also analyzed. The SSA of each model is calculated as one-absorbing AOD/AOD. The droplet number concentration for low clouds is obtained by the maximum value below 700-hPa level. The temporal coverage analyzed in this study is 1980–2014. Information of the selected CMIP6 models is listed in table S2.

AERONET data
We use AERONET observations as a reference of AOD trends. Level 2.0 monthly AOD products (64) at 440, 675, 870, and 1020 nm are used to represent observed AOD. To compare with CMIP6 models, AOD measured at the above four wavelengths is linearly interpolated to 550 nm on a logarithm scale (46). A monthly mean is considered valid only if there are more than five measurements for that month, and a year is considered valid when there are more than nine valid months. Stations with more than 10 valid years before 2014 are selected, and then the linear trend of AOD at each station is calculated from the monthly time series directly as the Sen's slope.

Description of HC
We use several metrics to describe the edge and strength of the HC (4, 34, 35, 65):

1) Ψ_{500}: Latitude where the zonal mean MMS at 500 hPa changes from positive to negative;

2) EDJ: Latitude of the maximum zonal mean zonal wind at 850 hPa;

3) SLP: Latitude of the maximum zonal mean SLP in the subtropics;

4) U_{srf}: Latitude where zonal mean surface zonal wind transitions from easterlies to westerlies;

5) OLR: First latitude where OLR drops to 20 W/m² below the peak value poleward of the subtropical OLR maximum.

The zonal mean MMS is computed as

$$\psi(p, \phi) = \frac{2\pi r \cos\phi}{g} \int_0^p <v> dp$$

where $\psi(p, \phi)$ is the MMS at pressure level p and latitude ϕ, r is the radius of the Earth, g is the gravitational acceleration, and $<v>$ is the zonal mean meridional wind. In general, positive MMS represents clockwise circulation. Following previous studies (44), we define the latitude at which MMS at 500 hPa reaches zero on the poleward side of the maximum MMS as the edge of the HC and the absolute value of the maximum MMS as the strength of the HC.

The zero-point latitudes used in the Ψ_{500} and the U_{srf} metrics are calculated using linear interpolation. The latitude of maximum 850-hPa zonal wind in the EDJ metric and maximum SLP in the SLP metric is identified as

$$\phi_{max} = \frac{\int_{\phi_1}^{\phi_2} F(\phi)^n \phi d\phi}{\int_{\phi_1}^{\phi_2} \phi d\phi}$$

where $F(\phi)$ is zonal mean 850-hPa zonal wind or SLP at each latitude and n is a smoothing parameter. Following previous studies, a parameter of $n = 6$ is chosen to provide accurate identification of maximum latitude in the NH (6, 65). Seasonal or annual mean

meridional wind, zonal wind at 850 hPa or at the surface, SLP, and OLR are calculated in the first step, and then the seasonal or annual mean NH HC edge based on these metrics is detected.

Trend estimation and significance test

The linear trends of meteorological fields as well as the HC edge and strength are calculated using the Sen's slope method (66). The Sen's slope b is calculated as

$$b = \text{Median}\left(\frac{X_i - X_j}{i - j}\right) \forall j < i$$

in which X_i and X_j are the values at the ith and the jth time step.

The significance level of the linear trends is calculated using the Mann-Kendall test (67, 68). The test statistic S is

$$S = \sum_{i}^{n-1} \sum_{j=i+1}^{n} \text{sgn}\left(X_j - X_i\right)$$

where n is the length of the time series, and sgn is the sign function.

The variance of S is

$$\text{Var}(S) = \frac{1}{18} n(n-1)(2n+5)$$

If $n > 30$, the standard normal test statistic ZS is

$$ZS = \begin{cases} \dfrac{S - 1}{\sqrt{\text{Var}(S)}} & \text{if } S > 0 \\[2mm] 0 & \text{if } S = 0 \\[2mm] \dfrac{S + 1}{\sqrt{\text{Var}(S)}} & \text{if } S < 0 \end{cases}$$

The trend is considered significant at the 95% confidence level if the absolute value of ZS is larger than 1.96.

The significance test of CESM experiments is performed using a two-sample t test. A bootstrapping is performed to the NH HC metrics in different simulations by collecting 50 subsamples to obtain the distributions of the mean value, and then the significance test is performed. To compare the results of CESM experiments with reanalysis datasets and CMIP6 simulations, the differences are divided by 3.7 assuming that the total time period is 37 years (1982–2019, midpoint of the two selected periods) so that the differences are converted into trends per decade.

The KE equation

We use the KE equation to diagnose contributions from different physical processes to the change of zonal mean MMS induced by aerosol forcing. The KE equation is based on thermal wind balance and quasi-geostrophic approximation, which is widely used to diagnose the change of HC strength (16, 39, 69, 70). See the Supplementary Materials for more details about the KE equation. With this equation, the change of zonal mean MSS can be decomposed into the changes of diabatic heating, static stability, eddy heat and momentum fluxes, zonal friction, and residual term.

Supplementary Materials

This PDF file includes:
Description of the Kuo-Eliassen equation
Tables S1 and S2
Figs. S1 to S14
References

REFERENCES AND NOTES

1. H. F. Diaz, R. S. Bradley, *The Hadley Circulation: Present, Past, and Future* (Kluwer Academic Publishers, 2004).
2. Y. Hu, Q. Fu, Observed poleward expansion of the Hadley circulation since 1979. *Atmos. Chem. Phys.* **7**, 5229–5236 (2007).
3. D. J. Seidel, W. J. Randel, Recent widening of the tropical belt: Evidence from tropopause observations. *J. Geophys. Res. Atmos.* **112**, D20113 (2007).
4. S. M. Davis, K. H. Rosenlof, A multidiagnostic intercomparison of tropical-width time series using reanalyses and satellite observations. *J. Clim.* **25**, 1061–1078 (2012).
5. Y. Y. Hu, H. Huang, C. Zhou, Widening and weakening of the Hadley circulation under global warming. *Sci. Bull.* **63**, 640–644 (2018).
6. K. M. Grise, S. M. Davis, P. W. Staten, O. Adam, Regional and seasonal characteristics of the recent expansion of the tropics. *J. Clim.* **31**, 6839–6856 (2018).
7. Y. Xia, Y. W. Wang, Y. Huang, Y. Y. Hu, J. C. Bian, C. F. Zhao, C. Sun, Significant contribution of stratospheric water vapor to the poleward expansion of the Hadley circulation in autumn under greenhouse warming. *Geophys. Res. Lett.* **48**, e2021GL094008 (2021).
8. P. W. Staten, J. Lu, K. M. Grise, S. M. Davis, T. Birner, Re-examining tropical expansion. *Nat. Clim. Change* **8**, 768–775 (2018).
9. R. J. Allen, J. R. Norris, M. Kovilakam, Influence of anthropogenic aerosols and the Pacific Decadal Oscillation on tropical belt width. *Nat. Geosci.* **7**, 270–274 (2014).
10. D. F. Mantsis, S. Sherwood, R. Allen, L. Shi, Natural variations of tropical width and recent trends. *Geophys. Res. Lett.* **44**, 3825–3832 (2017).
11. R. J. Allen, M. Kovilakam, The role of natural climate variability in recent tropical expansion. *J. Clim.* **30**, 6329–6350 (2017).
12. K. M. Grise, S. M. Davis, I. R. Simpson, D. W. Waugh, Q. Fu, R. J. Allen, K. H. Rosenlof, C. C. Ummenhofer, K. B. Karnauskas, A. C. Maycock, X. W. Quan, T. Birner, P. W. Staten, Recent tropical expansion: Natural variability or forced response? *J. Clim.* **32**, 1551–1571 (2019).
13. R. Chemke, J. Yuval, Human-induced weakening of the Northern Hemisphere tropical circulation. *Nature* **617**, 529–532 (2023).
14. J. Lu, G. A. Vecchi, T. Reichler, Expansion of the Hadley cell under global warming. *Geophys. Res. Lett.* **34**, L06805 (2007).
15. R. Chemke, L. M. Polvani, Exploiting the abrupt 4 x CO₂ scenario to elucidate tropical expansion mechanisms. *J. Clim.* **32**, 859–875 (2019).
16. R. Chemke, L. M. Polvani, Elucidating the mechanisms responsible for Hadley cell weakening under 4 × CO₂ forcing. *Geophys. Res. Lett.* **48**, e2020GL090348 (2021).
17. L. J. Tao, Y. Y. Hu, J. P. Liu, Anthropogenic forcing on the Hadley circulation in CMIP5 simulations. *Clim. Dyn.* **46**, 3337–3350 (2016).
18. S. K. Min, S. W. Son, Multimodel attribution of the Southern Hemisphere Hadley cell widening: Major role of ozone depletion. *J. Geophys. Res.* **118**, 3007–3015 (2013).
19. S. W. Son, N. F. Tandon, L. M. Polvani, D. W. Waugh, Ozone hole and Southern Hemisphere climate change. *Geophys. Res. Lett.* **36**, L15705 (2009).
20. L. M. Polvani, D. W. Waugh, G. J. P. Correa, S. W. Son, Stratospheric ozone depletion: The main driver of twentieth-century atmospheric circulation changes in the Southern Hemisphere. *J. Clim.* **24**, 795–812 (2011).
21. S. W. Son, E. P. Gerber, J. Perlwitz, L. M. Polvani, N. P. Gillett, K. H. Seo, V. Eyring, T. G. Shepherd, D. Waugh, H. Akiyoshi, J. Austin, A. Baumgaertner, S. Bekki, P. Braesicke, C. Bruhl, N. Butchart, M. P. Chipperfield, D. Cugnet, M. Dameris, S. Dhomse, S. Frith, H. Garny, R. Garcia, S. C. Hardiman, P. Jockel, J. F. Lamarque, E. Mancini, M. Marchand, M. Michou, T. Nakamura, O. Morgenstern, G. Pitari, D. A. Plummer, J. Pyle, E. Rozanov, J. F. Scinocca, K. Shibata, D. Smale, H. Teyssedre, W. Tian, Y. Yamashita, Impact of stratospheric ozone on Southern Hemisphere circulation change: A multimodel assessment. *J. Geophys. Res.* **115**, D00M07 (2010).
22. A. Robock, T. Adams, M. Moore, L. Oman, G. Stenchikov, Southern Hemisphere atmospheric circulation effects of the 1991 Mount Pinatubo eruption. *Geophys. Res. Lett.* **34**, L23710 (2007).
23. R. J. Allen, S. C. Sherwood, J. R. Norris, C. S. Zender, Recent Northern Hemisphere tropical expansion primarily driven by black carbon and tropospheric ozone. *Nature* **485**, 350–354 (2012).
24. S. Szopa, V. Naik, B. Adhikary, P. Artaxo, T. Berntsen, W. D. Collins, S. Fuzzi, L. Gallardo, A. Kiendler-Scharr, Z. Klimont, H. Liao, N. Unger, P. Zanis, "Short-lived climate forcers" in *Climate Change 2021: The Physical Science Basis. Contribution of Working Group I to the Sixth Assessment Report of the Intergovernmental Panel on Climate Change* (Cambridge Univ. Press, 2021).

25. X. Y. Zhao, R. J. Allen, T. Wood, A. C. Maycock, Tropical belt width proportionately more sensitive to aerosols than greenhouse gases. *Geophys. Res. Lett.* **47**, e2019GL086425 (2020).

26. Y. Wang, J. H. Jiang, H. Su, Atmospheric responses to the redistribution of anthropogenic aerosols. *J. Geophys. Res.* **120**, 9625–9641 (2015).

27. J. Li, B. E. Carlson, Y. L. Yung, D. R. Lv, J. Hansen, J. E. Penner, H. Liao, V. Ramaswamy, R. A. Kahn, P. Zhang, O. Dubovik, A. J. Ding, A. A. Lacis, L. Zhang, Y. M. Dong, Scattering and absorbing aerosols in the climate system. *Nat. Rev. Earth Environ.* **3**, 363–379 (2022).

28. R. J. Allen, O. Ajoku, Future aerosol reductions and widening of the northern tropical belt. *J. Geophys. Res.* **121**, 6765–6786 (2016).

29. X. Q. Li, M. F. Ting, D. E. Lee, Fast adjustments of the Asian summer monsoon to anthropogenic aerosols. *Geophys. Res. Lett.* **45**, 1001–1010 (2018).

30. B. S. Grandey, H. W. Cheng, C. Wang, Transient climate impacts for scenarios of aerosol emissions from Asia: A story of coal versus gas. *J. Clim.* **29**, 2849–2867 (2016).

31. J. K. P. Shonk, A. G. Turner, A. Chevuturi, L. J. Wilcox, A. J. Dittus, E. Hawkins, Uncertainty in aerosol radiative forcing impacts the simulated global monsoon in the 20th century. *Atmos. Chem. Phys.* **20**, 14903–14915 (2020).

32. Z. Y. Shen, Y. Ming, The influence of aerosol absorption on the extratropical circulation. *J. Clim.* **31**, 5961–5975 (2018).

33. D. M. Westervelt, Y. J. You, X. Q. Li, M. F. Ting, D. E. Lee, Y. Ming, Relative importance of greenhouse gases, sulfate, organic carbon, and black carbon aerosol for South Asian monsoon rainfall changes. *Geophys. Res. Lett.* **47**, e2020GL088363 (2020).

34. D. W. Waugh, K. M. Grise, W. J. M. Seviour, S. M. Davis, N. Davis, O. Adam, S. W. Son, I. R. Simpson, P. W. Staten, A. C. Maycock, C. C. Ummenhofer, T. Birner, A. Ming, Revisiting the relationship among metrics of tropical expansion. *J. Clim.* **31**, 7565–7581 (2018).

35. N. Davis, T. Birner, On the discrepancies in tropical belt expansion between reanalyses and climate models and among tropical belt width metrics. *J. Clim.* **30**, 1211–1231 (2017).

36. O. Watt-Meyer, D. M. W. Frierson, Q. Fu, Hemispheric asymmetry of tropical expansion under CO_2 forcing. *Geophys. Res. Lett.* **46**, 9231–9240 (2019).

37. G. A. Vecchi, B. J. Soden, Global warming and the weakening of the tropical circulation. *J. Clim.* **20**, 4316–4340 (2007).

38. S. Bony, G. Bellon, D. Klocke, S. Sherwood, S. Fermepin, S. Denvil, Robust direct effect of carbon dioxide on tropical circulation and regional precipitation. *Nat. Geosci.* **6**, 447–451 (2013).

39. R. Chemke, L. M. Polvani, Opposite tropical circulation trends in climate models and in reanalyses. *Nat. Geosci.* **12**, 528–532 (2019).

40. R. J. Allen, S. C. Sherwood, J. R. Norris, C. S. Zender, The equilibrium response to idealized thermal forcings in a comprehensive GCM: Implications for recent tropical expansion. *Atmos. Chem. Phys.* **12**, 4795–4816 (2012).

41. J. Li, Y. W. Jiang, X. G. Xia, Y. Y. Hu, Increase of surface solar irradiance across East China related to changes in aerosol properties during the past decade. *Environ. Res. Lett.* **13**, 034006 (2018).

42. M. A. Obregon, M. J. Costa, A. M. Silva, A. Serrano, Impact of aerosol and water vapour on SW radiation at the surface: Sensitivity study and applications. *Atmos. Res.* **213**, 252–263 (2018).

43. F. Q. Lu, S. Y. Chen, Z. Y. Hu, Z. W. Han, K. Alam, H. Y. Luo, H. R. Bi, J. Y. Chen, X. Y. Guo, Sensitivity and uncertainties assessment in radiative forcing due to aerosol optical properties in diverse locations in China. *Sci. Total Environ.* **860**, 160447 (2023).

44. Y. Xia, Y. Y. Hu, J. P. Liu, Comparison of trends in the Hadley circulation between CMIP6 and CMIP5. *Sci. Bull.* **65**, 1667–1674 (2020).

45. K. M. Grise, S. M. Davis, Hadley cell expansion in CMIP6 models. *Atmos. Chem. Phys.* **20**, 5249–5268 (2020).

46. J. Li, B. E. Carlson, O. Dubovik, A. A. Lacis, Recent trends in aerosol optical properties derived from AERONET measurements. *Atmos. Chem. Phys.* **14**, 12271–12289 (2014).

47. J. Feichter, E. Roeckner, U. Lohmann, B. Liepert, Nonlinear aspects of the climate response to greenhouse gas and aerosol forcing. *J. Clim.* **17**, 2384–2398 (2004).

48. J. C. Deng, A. G. Dai, H. M. Xu, Nonlinear climate responses to increasing CO_2 and anthropogenic aerosols simulated by CESM1. *J. Clim.* **33**, 281–301 (2020).

49. S. Ramachandran, M. Rupakheti, R. Cherian, Insights into recent aerosol trends over Asia from observations and CMIP6 simulations. *Sci. Total Environ.* **807**, 150756 (2022).

50. O. Dubovik, Z. Q. Li, M. I. Mishchenko, D. Tanre, Y. Karol, B. Bojkov, B. Cairns, D. J. Diner, W. R. Espinosa, P. Goloub, X. F. Gu, O. Hasekamp, J. Hong, W. Z. Hou, K. D. Knobelspiesse, J. Landgraf, L. Li, P. Litvinov, Y. Liu, A. Lopatin, T. Marbach, H. Maring, V. Martins, Y. Meijer, G. Milinevsky, S. Mukai, F. Parol, Y. L. Qiao, L. Remer, J. Rietjens, I. Sano, P. Stammes, S. Stamnes, X. B. Sun, P. Tabary, L. D. Travis, F. Waquet, F. Xu, C. X. Yan, D. K. Yin, Polarimetric remote sensing of atmospheric aerosols: Instruments, methodologies, results, and perspectives. *J. Quant. Spectrosc. Radiat. Transf.* **224**, 474–511 (2019).

51. N. Schutgens, O. Dubovik, O. Hasekamp, O. Torres, H. Jethva, P. J. T. Leonard, P. Litvinov, J. Redemann, Y. Shinozuka, G. de Leeuw, S. Kinne, T. Popp, M. Schulz, P. Stier, AEROCOM and AEROSAT AAOD and SSA study – Part 1: Evaluation and intercomparison of satellite measurements. *Atmos. Chem. Phys.* **21**, 6895–6917 (2021).

52. R. A. Kahn, E. Andrews, C. A. Brock, M. Chin, G. Feingold, A. Gettelman, R. C. Levy, D. M. Murphy, A. Nenes, J. R. Pierce, T. Popp, J. Redemann, A. M. Sayer, A. M. da Silva, L. Sogacheva, P. Stier, Reducing aerosol forcing uncertainty by combining models with satellite and within-the-atmosphere observations: A three-way street. *Rev. Geophys.* **61**, e2022RG000796 (2023).

53. H. Hersbach, B. Bell, P. Berrisford, S. Hirahara, A. Horanyi, J. Munoz-Sabater, J. Nicolas, C. Peubey, R. Radu, D. Schepers, A. Simmons, C. Soci, S. Abdalla, X. Abellan, G. Balsamo, P. Bechtold, G. Biavati, J. Bidlot, M. Bonavita, G. De Chiara, P. Dahlgren, D. Dee, M. Diamantakis, R. Dragani, J. Flemming, R. Forbes, M. Fuentes, A. Geer, L. Haimberger, S. Healy, R. J. Hogan, E. Holm, M. Janiskova, S. Keeley, P. Laloyaux, P. Lopez, C. Lupu, G. Radnoti, P. de Rosnay, I. Rozum, F. Vamborg, S. Villaume, J.-N. Thepaut, The ERA5 global reanalysis. *Q. J. R. Meteor. Soc.* **146**, 1999–2049 (2020).

54. R. Gelaro, W. McCarty, M. J. Suarez, R. Todling, A. Molod, L. Takacs, C. A. Randles, A. Darmenov, M. G. Bosilovich, R. Reichle, K. Wargan, L. Coy, R. Cullather, C. Draper, S. Akella, V. Buchard, A. Conaty, A. M. da Silva, W. Gu, G. K. Kim, R. Koster, R. Lucchesi, D. Merkova, J. E. Nielsen, G. Partyka, S. Pawson, W. Putman, M. Rienecker, S. D. Schubert, M. Sienkiewicz, B. Zhao, The modern-era retrospective analysis for research and applications, version 2 (MERRA-2). *J. Clim.* **30**, 5419–5454 (2017).

55. C. A. Randles, A. M. da Silva, V. Buchard, P. R. Colarco, A. Darmenov, R. Govindaraju, A. Smirnov, B. Holben, R. Ferrare, J. Hair, Y. Shinozuka, C. J. Flynn, The MERRA-2 aerosol reanalysis, 1980 Onward. Part I: System description and data assimilation evaluation. *J. Clim.* **30**, 6823–6850 (2017).

56. J. W. Hurrell, M. M. Holland, P. R. Gent, S. Ghan, J. E. Kay, P. J. Kushner, J. F. Lamarque, W. G. Large, D. Lawrence, K. Lindsay, W. H. Lipscomb, M. C. Long, N. Mahowald, D. R. Marsh, R. B. Neale, P. Rasch, S. Vavrus, M. Vertenstein, D. Bader, W. D. Collins, J. J. Hack, J. Kiehl, S. Marshall, The community earth system model: A framework for collaborative research. *Bull. Am. Meteorol. Soc.* **94**, 1339–1360 (2013).

57. X. Lan, P. Tans, K. W. Thoning, Trends in globally-averaged CO2 determined from NOAA Global monitoring laboratory measurements, version 2024-10, NOAA Global Monitoring Laboratory (2023); https://doi.org/10.15138/9N0H-ZH07.

58. G. S. Dutton, B. D. Hall, S. A. Montzka, J. D. Nance, Combined atmospheric chlorofluorocarbon-11 dry air mole fractions from the NOAA GML halocarbons sampling network, version 2023-04-13, NOAA Global Monitoring Laboratory (2023); https://doi.org/10.15138/BVQ6-2S69.

59. G. S. Dutton, B. D. Hall, S. A. Montzka, J. D. Nance, Combined atmospheric chlorofluorocarbon-12 dry air mole fractions from the NOAA GML halocarbons sampling network, version 2023-04-13, NOAA Global Monitoring Laboratory (2023); https://doi.org/10.15138/PJ63-H440.

60. G. S. Dutton, B. D. Hall, E. J. Dlugokencky, X. Lan, J. D. Nance, M. Madronich, Combined atmospheric nitrous oxide dry air mole fractions from the NOAA GML halocarbons sampling network, version 2023-04-13, NOAA Global Monitoring Laboratory (2023); https://doi.org/10.15138/GMZ7-2Q16.

61. X. Lan, K. W. Thoning, E. J. Dlugokencky, Trends in globally-averaged CH4, N2O, and SF6 determined from NOAA Global Monitoring Laboratory measurements, version 2024-10, NOAA Global Monitoring Laboratory (2022); https://doi.org/10.15138/P8XG-AA10.

62. V. Eyring, S. Bony, G. A. Meehl, C. A. Senior, B. Stevens, R. J. Stouffer, K. E. Taylor, Overview of the coupled model intercomparison project phase 6 (CMIP6) experimental design and organization. *Geosci. Model Dev.* **9**, 1937–1958 (2016).

63. N. P. Gillett, H. Shiogama, B. Funke, G. Hegerl, R. Knutti, K. Matthes, B. D. Santer, D. Stone, C. Tebaldi, The detection and attribution model intercomparison project (DAMIP v1.0) contribution to CMIP6. *Geosci. Model Dev.* **9**, 3685–3697 (2016).

64. D. M. Giles, A. Sinyuk, M. G. Sorokin, J. S. Schafer, A. Smirnov, I. Slutsker, T. F. Eck, B. N. Holben, J. R. Lewis, J. R. Campbell, E. J. Welton, S. V. Korkin, A. I. Lyapustin, Advancements in the aerosol robotic network (AERONET) version 3 database - automated near-real-time quality control algorithm with improved cloud screening for Sun photometer aerosol optical depth (AOD) measurements. *Atmos. Meas. Tech.* **12**, 169–209 (2019).

65. O. Adam, K. M. Grise, P. Staten, I. R. Simpson, S. M. Davis, N. A. Davis, D. W. Waugh, T. Birner, A. Ming, The TropD software package (v1): Standardized methods for calculating tropical-width diagnostics. *Geosci. Model Dev.* **11**, 4339–4357 (2018).

66. P. K. Sen, Estimates of the regression coefficient based on Kendall's tau. *J. Am. Stat. Assoc.* **63**, 1379–1389 (1968).

67. H. B. Mann, Nonparametric tests against trend. *Econometrica* **13**, 245–259 (1945).

68. M. G. Kendall, *Rank Correlation Methods* (Griffin, 1975).

69. S. Y. Zhang, Y. Y. Hu, J. Yang, X. Li, W. Y. Kang, J. Zhang, Y. G. Liu, J. Nie, The Hadley circulation in the Pangea era. *Sci. Bull.* **68**, 1060–1068 (2023).

70. O. Hess, R. Chemke, Anthropogenic forcings reverse a simulated multi-century naturally-forced Northern Hemisphere Hadley cell intensification. *Nat. Commun.* **15**, 4001 (2024).

71. G. Danabasoglu, NCAR CESM2 model output prepared for CMIP6 CMIP historical, version 20190401, Earth System Grid Federation (2019); https://doi.org/10.22033/ESGF/CMIP6.7627.

72. A. Vordoire, CMIP6 simulations of the CNRM-CERFACS based on CNRM-CM6-1 model for CMIP experiment historical, version 20180917, Earth System Grid Federation (2018); https://doi.org/10.22033/ESGF/CMIP6.4066.

73. NASA Goddard Institute for Space Studies (NASA/GISS), NASA-GISS GISS-E2.1G model output prepared for CMIP6 CMIP historical, version 20190908, Earth System Grid Federation (2018); https://doi.org/10.22033/ESGF/CMIP6.6109.

74. J. Ridley, M. Menary, T. Kuhlbrodt, M. Andrews, T. Andrews, MOHC HadGEM3-GC31-LL model output prepared for CMIP6 CMIP historical, version 20190624, Earth System Grid Federation (2019); https://doi.org/10.22033/ESGF/CMIP6.6109.

75. O. Boucher, S. Denvil, G. Levavasseur, A. Cozic, A. Caubel, M.-A. Foujols, Y. Meurdesoif, C. Ethé, J. Deshayes, IPSL IPSL-CM6A-LR model output prepared for CMIP6 CMIP historical, version 20180803, Earth System Grid Federation (2018); https://doi.org/10.22033/ESGF/CMIP6.5195.

76. H. Tatebe, M. Watanabe, MIROC MIROC6 model output prepared for CMIP6 CMIP historical, version 20181212, Earth System Grid Federation (2018); https://doi.org/10.22033/ESGF/CMIP6.5603.

77. S. Yukimoto, T. Koshiro, H. Kawai, N. Oshima, K. Yoshida, S. Urakawa, H. Tsujino, M. Deushi, T. Tanaka, M. Hosaka, H. Yoshimura, E. Shindo, R. Mizuta, M. Ishii, A. Obata, Y. Adachi, MRI MRI-ESM2.0 model output prepared for CMIP6 CMIP historical, version 20190222, Earth System Grid Federation (2019); https://doi.org/10.22033/ESGF/CMIP6.6842.

78. Ø. Seland, M. Bentsen, D. J. L. Oliviè, T. Toniazzo, A. Gjermundsen, L. S. Graff, J. B. Debernard, A. K. Gupta, Y. He, A. Kirkevåg, J. Schwinger, J. Tjiputra, K. S. Aas, I. Bethke, Y. Fan, J. Griesfeller, A. Grini, C. Guo, M. Ilicak, I. H. H. Karset, NCC NorESM2-LM model output prepared for CMIP6 CMIP historical, version 20190920, Earth System Grid Federation (2019); https://doi.org/10.22033/ESGF/CMIP6.8036.